Continental Shelf Research 29 (2009) 1373–1383

Contents lists available at ScienceDirect

Continental Shelf Research

journal homepage: www.elsevier.com/locate/csr

The variability of the large-amplitude internal wave field on the Australian North West Shelf

Paul Van Gastel [a,*], Gregory N. Ivey [a], Michael J. Meuleners [a], Jason P. Antenucci [b], Oliver Fringer [c]

[a] School of Environmental Systems Engineering, University of Western Australia, Crawley, Western Australia 6009, Australia
[b] Centre for Water Research, University of Western Australia, Crawley, Western Australia 6009, Australia
[c] Department of Civil and Environmental Engineering, Stanford University, Palo Alto, CA, USA

ARTICLE INFO

Article history:
Received 24 July 2008
Received in revised form
21 January 2009
Accepted 3 February 2009
Available online 27 February 2009

Keywords:
Internal waves
Solitary waves
Internal tide
Continental slope
Australian North West Shelf (14–22°S, 114–126°E)

ABSTRACT

Observations are presented of large-amplitude internal waves (LAIWs) generated by the steepening of the internal tide on the Australian North West Shelf (NWS) over a 4-month period extending from strongly stratified summer conditions to weakly stratified winter conditions. The observations are from a site in water depth of 124 m where current and temperature measurements were made from a fixed vertical mooring and a benthic L-shaped spatial array. The observations show the LAIWs at this site to be characterized by strong seasonal variability, with energetic LAIWs of depression being dominant during summer and weaker LAIWs of elevation being dominant during the winter months as the stratification weakens, the upper mixed layer deepens, and the thermocline is close to the bottom. Waves were also seen to propagate from a range of directions towards the observation site. Modeling using the Regional Ocean Modeling System (ROMS v2.1) revealed that internal tide generation in the area occurred at water depths of between 400 and 600 m along an arc of approximately 120 km in length, some 70 km to the northwest of our experimental site. The results demonstrate both the 3D nature as well as the seasonal variation of the LAIW field.

1. Introduction

On the North West Shelf (NWS), tidal amplitudes range up to 10 m and the magnitude of the dissipation of tidal energy is one of the strongest on the globe (e.g. Egbert and Ray, 2000). The continental shelf edge is defined as the 400 m contour, beyond which the bathymetry steepens considerably to a depth of over 1200 m (Fig. 1). Tides in the region are semidiurnal with a small diurnal inequality and this combination of strong tide, steep topography and year-round density stratification due to the strong solar heating generates considerable internal wave activity.

It is known that internal waves of tidal frequency or internal tides are generated by the interaction of barotropic tidal currents with sloping topography in the presence of density stratification at critical points when the slope of the internal wave characteristics equals the bottom slope (e.g. Vlasenko et al., 2005). These critical points are known as generation sites where beams of energy are predicted to emanate in both the shoreward and seaward directions (New and Pingree, 1990). One concept is that IW packets will form by nonlinear steepening of the linear internal tide by the shoreward propagation over the sloping bottom of the continental slope (Vlasenko et al., 2005). During the shoreward propagation the wave packet is continually modified as the number of oscillations increases and the wave amplitude grows.

Using satellite imagery, Baines (1981) was the first to identify the existence of these internal waves structures propagating shoreward across the NWS. Although Baines could not identify the physical characteristics of these wave packets, Holloway (1983, 1984, 1987) using direct in-situ observations showed the existence of large-amplitude semidiurnal internal waves on the NWS, propagating in the onshore direction across perpendicular to the bathymetry (roughly NW–SE direction) and revealed a substantial seasonal variability in the semidiurnal internal tide over timescales of weeks to months. The most recent field observations, reported by Holloway et al. (2001) from measurements near the North Rankin A (NRA) oil and gas platform, were made between January and February 1995 during the strongly stratified summer period. Their results suggested critical internal tide generation sites exist on the NWS offshore from NRA near depths of 200 and 600 m, consistent with earlier results of Craig (1988).

There have also been efforts to apply weakly nonlinear wave extended KdV theory to describe the observed waved forms on the NWS (for example, Smyth and Holloway, 1988; Holloway et al., 1997, 1999; Grimshaw et al., 2004). They noted that the nonlinear

* Corresponding author.
E-mail address: vangaste@sese.uwa.edu.au (P. Van Gastel).

0278-4343/$ - see front matter © 2009 Elsevier Ltd. All rights reserved.
doi:10.1016/j.csr.2009.02.006

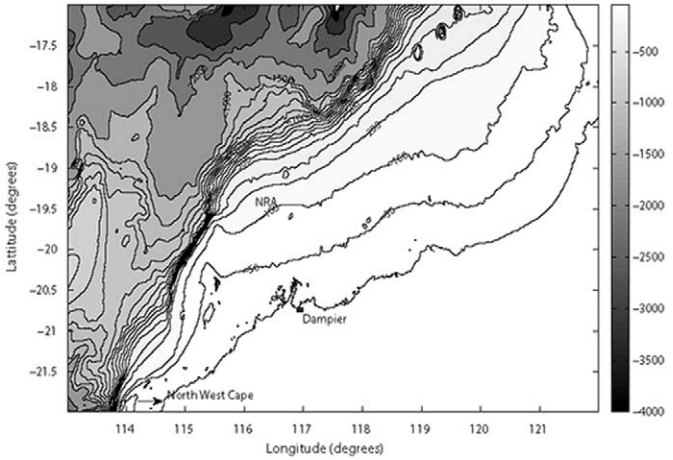

Fig. 1. The North West Shelf of Australia. Bathymetry and the location of North Rankin A (NRA) platform are shown.

terms (both quadratic and cubic) are small off the shelf but become significant only in a relatively small region across the shelf. Vlasenko and Stashchuk (2007) suggest the applicability of such weakly nonlinear theories to large-amplitude internal waves (LAIWs) is debatable, and that it is difficult to apply such theories to cases where significant three-dimensional effects can occur.

Although there have been numerous studies of internal tides near continental margins [see Huthnance (1989) for a review] most studies have excluded three-dimensional effects. Holloway (1996) using the hydrostatic fully nonlinear Princeton Ocean Model (POM) demonstrated the three-dimensional nature of the internal tide. Using a depth integrated forcing function he found that the contribution of the alongshelf topographical gradients in generating the internal tide to be approximately 10% of the more dominant cross-shelf component.

It remains unclear from previous work in the region what is the spatial and temporal variability in the internal wave field, and how significant three-dimensional effects are on generation and wave propagation on the NWS. In this paper we address some of these issues. We describe results from an extensive and continuous 4-month-long field experiment conducted in 2004 at the NRA field site. Measurements include both through the water column measurements and an L-shaped benthic current meter array designed to give, for the first time, a detailed look at the variability and directional characteristics of the LAIWs on the NWS. These results are combined with the results from a numerical experiment using a free-surface, hydrostatic primitive equation model to elucidate the processes important in the generation and propagation of the internal wave field towards the experimental site. The remainder of the paper is organized as follows. In Section 2, the experimental site and methodology is described, while the analysis of the field data and numerical modeling data is presented in Section 3. Finally in Section 4 the conclusions are presented.

2. Methodology

2.1. Field measurements

During the early 1990s our main industry partner observed strong near seabed currents in the vicinity of the NRA platform. Concerned about the stability of their subsurface pipelines they decided to establish a long-term monitoring program, and in the mid-1990s established a through water column (TWC) current meter array adjacent to the NRA platform (latitude 19.6°S, longitude 116.14°E). The array consisted of 6 acoustic current meters suspended on a taut wire extending from the base of the NRA flare tower to the seabed in a nominal water depth of 124 m. Temperature and current magnitude and direction (relative to magnetic north) were recorded at a 2 min sampling rate and measurements were made at heights of 5, 30, 60, 75, 102 and 117.5 m above the sea bottom. Through the initial analysis of this data, an internal wave field experiment was devised consisting of the TWC current meter array at NRA and the establishment of an L-shaped benthic array to record from the 11th March, 2004 until 21st June, 2004. The benthic L-shaped array was designed to provide information about the horizontal structure of the internal tide, and contained six cross-shelf (CS1 to CS6) and seven long-shelf (LS1 to LS7) moorings along two orthogonal lines radiating on a northwesterly (cross-shore, 313°TN) and northeasterly (alongshore, 43°TN) bearing from the NRA platform. The long axis of the array was aligned with the major axis of the local tidal ellipse determined from the TWC measurements. Moorings were spaced between 50 and 200 m apart and each mooring carried a single current meter at 2.5 m above sea bottom (Fig. 2). All instruments on the L-shaped array collected temperature and current magnitude and direction measurements at 1 min sampling enabling both the phase speed and direction of the internal tide to be estimated.

2.2. Numerical model setup

To assist in the interpretation of these field measurements, the Regional Ocean Modeling System (ROMS) v2.1 (Haidvogel et al., 2000; Shchepetkin and McWilliams, 2005) was run on a domain of approximately 800 km by 500 km with the field site within the computational domain. ROMS is a hydrostatic, primitive equation ocean model that solves the Reynolds averaged form of the Navier–Stokes equations on an Arakawa "C" grid and uses stretched terrain following (sigma) coordinates in the vertical. The model can be configured with choices from several types of boundary conditions, horizontal and vertical advection schemes for momentum and tracers, pressure-gradient algorithms and turbulence closures. We configure the model's horizontal advective scheme using a third-order, upstream-bias G-scheme and a spline advection scheme for vertical transport. The parameterization of vertical turbulent mixing for momentum and tracers is based on Mellor Yamada 2.5 order closure model (Mellor and Yamada, 1982) and the horizontal eddy coefficient used for momentum and tracers adopted a Laplacian parameterization.

The model domain consisted of three open boundaries located on the study area's northern, southern and western extents (Fig. 3). Representation of the internal forcing was accomplished by maintaining a temporally varying boundary condition for temperature and salinity at all open boundaries. Radiation boundary conditions were prescribed for the baroclinic tracers. The forcing data was sourced from the Bluelink ReANalysis (BRAN) version 2.1, which was developed for the purposes of ocean reanalyses and ocean forecasting around Australia (Oke et al., 2008). The BRAN data consists of daily averaged snapshots of the baroclinic variables at a horizontal resolution of 10 km. Tidal forcing was applied using the Ohio State University TPXO.6.2 global tidal solution with a 0.25° horizontal resolution. The M2, S2, N2, K2, O1, K1, P1 and Q1 tidal constituents were applied. Wind forcing was applied using daily averaged blended vector sea surface winds (at 10 m above sea level). The blended winds are from multiple satellite observations, on a global 0.25° grid sourced from the National Climatic Data Center (NCDC). Thermodynamic forcing data was obtained from the National Oceanic and Atmospheric Administration NCEP/NCAR reanalysis data set.

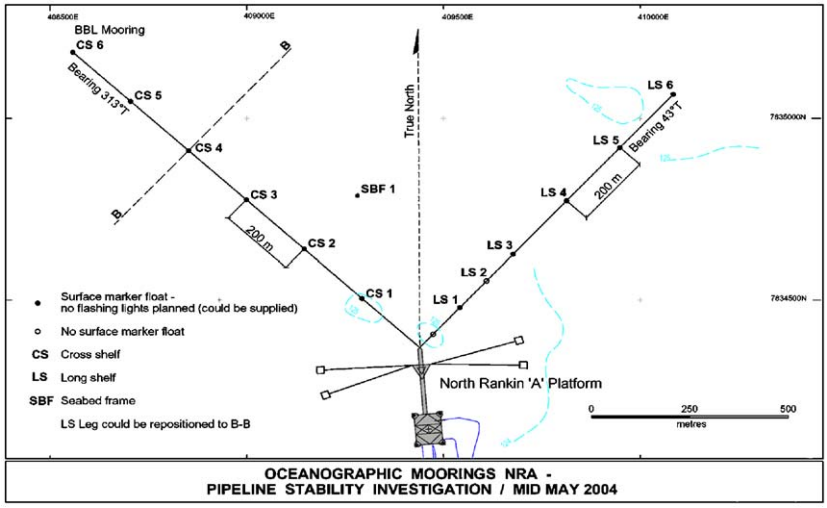

Fig. 2. Schematic diagram of the current meter mooring at NRA showing a cross shore array, an alongshore array, a seabed frame and the distances between the moorings.

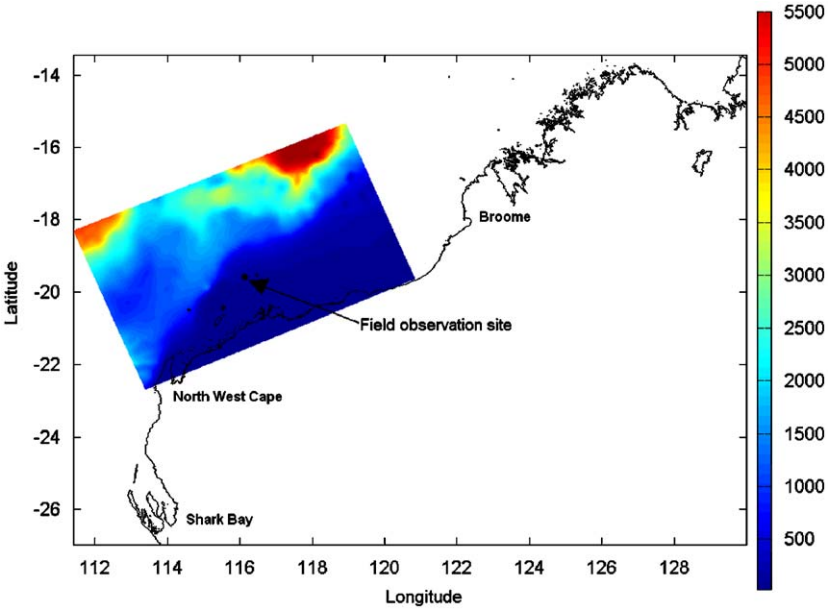

Fig. 3. The modeled domain for the ROMS simulations.

The model domain extends ~800 km in an alongshore direction and ~500 km in a cross-shore direction with the horizontal resolution set to a nominal 2.5 km in the east/west and north/south directions. Geoscience Australia (GA) provided the bathymetric data at the nominal resolution of 1 km. The model domain's minimum depth was set to 20 m and the number of vertical sigma layers was set to 50, with increased resolution in the near-surface and near seabed layers. The bottom stress was computed using a quadratic bottom drag coefficient (Table 1). A comprehensive discussion of the model and its application to the NWS and the effects of mesoscale dynamics are found in Van Gastel et al. (2009). Here we discuss only the results of a simulation commenced on the 13th March, 2004 and run for 60 days—thus covering the first two months of the field experiment where the ambient stratification was the strongest. The density-driven solution evolved for approximately five days at which time the volume-averaged kinetic energy reached a quasi-steady-state balance and the solution thereafter was assessed quantitatively.

Table 1
Model parameterization.

Δx, M	2.5 km, 200	Resolution zonal direction, number of grid points
Δy, L	2.5 km, 300	Resolution meridional direction, number of grid points
N	50	Number of sigma coordinate levels
h_{max}	>4000 m	Maximum depth of computational domain
h_{min}	20 m	Minimum depth of computational domain
θ_s	3.0	Sigma coordinate stretching factor
θ_b	0.9	Sigma coordinate bottom stretching factor
Δt(baroclinic)	200 s	Baroclinic time step
Δt(barotropic)	2 s	Barotropic time step
ν_v	4.6 m^2/s	Horizontal eddy viscosity
ν_d	4.6 m^2/s	Horizontal eddy diffusivity
r	2.5×10^{-3}	Quadratic bottom drag coefficient

2.3. Model runs

Two model runs were performed each with the same model setup and forcing described in Section 2.2 but run over a different

time period. The model runs were initiated from rest and to assist in the interpretation of the field observations the primary simulation commenced on the 13th March, 2004 and ran for 60 days. The second simulation was performed to assist in model verification and commenced on the 1st January, 2000 and ran for 40 days and this period coincided with periods of available the sea surface height recordings at NRA. The simulations presented here were performed on an SGI high-performance computer using Open MP directives. Approximately 15 h (real time) using 8 cpu's were required to complete the primary simulation.

3. Results

3.1. Field observations

The CTD profiles revealed near constant salinity of 34.91 psu, and thus temperature was the dominant effect on density. The seasonal variability in the temperature in the water column was investigated using time series from the six moorings over the depth at the NRA flare tower. Temperature was interpolated vertically to a 1 m resolution using a cubic spline interpolation and the temperature data was passed through a 30 h low-pass filter to remove the tidal signals, and in Fig. 4 we also plot the mean temperature profile and buoyancy frequency profile over four different time segments which are representative of each month of the deployment. During the late summer months (March and April), the ocean is continuously and strongly stratified. In March (Fig. 4a) and April (Fig. 4b) the mean temperature profiles are close to linear gradients from top to bottom, giving an almost constant buoyancy frequency, although in April there is evidence of a stronger near-bottom stratification. In May (Fig. 4c), the water column is mixed to a depth of approximately 60 m as the stratification is eroded from the surface downwards due to seasonal surface cooling and wind mixing. In June (Fig. 4d) the water column is mixed nearly to completion.

These seasonal changes in stratification produce seasonal changes in the character of the internal waves observed at NRA and Fig. 5 shows four different but representative examples of waveforms observed during the mooring period. Fig. 5a is from 13th of March shows depression of the near-surface isotherms as an internal bore accompanied by a train of internal solitary waves, followed in turn by a wave train of elevation leads to a final recovery of the isotherms to the initial near-surface position. Generally such bores induce the strongest bottom currents in excess of 1.1 m/s. Fig. 5b shows another example of a bore followed several hours later by a solitary wave train of elevation, similar to the shock waves observed by Smyth and Holloway (1988). The most common waveform in our data set is the disturbance shown in Fig. 5c whereby a bore is followed by a solitary wave packet, without any secondary dispersive wave tail. There is, instead, a near-linear relaxation of the isopycnals back towards the original depth. Due to seasonal cooling, from 12 April on the thermocline is located below mid-depth and only LAIWs of elevation were subsequently observed at the NRA field site. The final wave example shown in Fig. 5d was observed in the month of May and shows a train of individual LAIWs of elevation that travel along the interface between a deep well-mixed upper layer and a relatively thin strongly stratified lower layer. LAIWs were almost nonexistent during the winter months with near homogeneous density stratification (June).

Over the entire record, these LAIW packets had timescales ranging from 1.5 h down to 12 min. Currents of magnitude up to 1.0 m/s (see Fig. 6) were induced near the seabed during the passage of the packet. The passage of the packets occurred on approximately a semidiurnal timescale (12.4 h) consistent with the onshore propagation of the internal tide although the arrival time varied between 11.3 and 13.5 h.

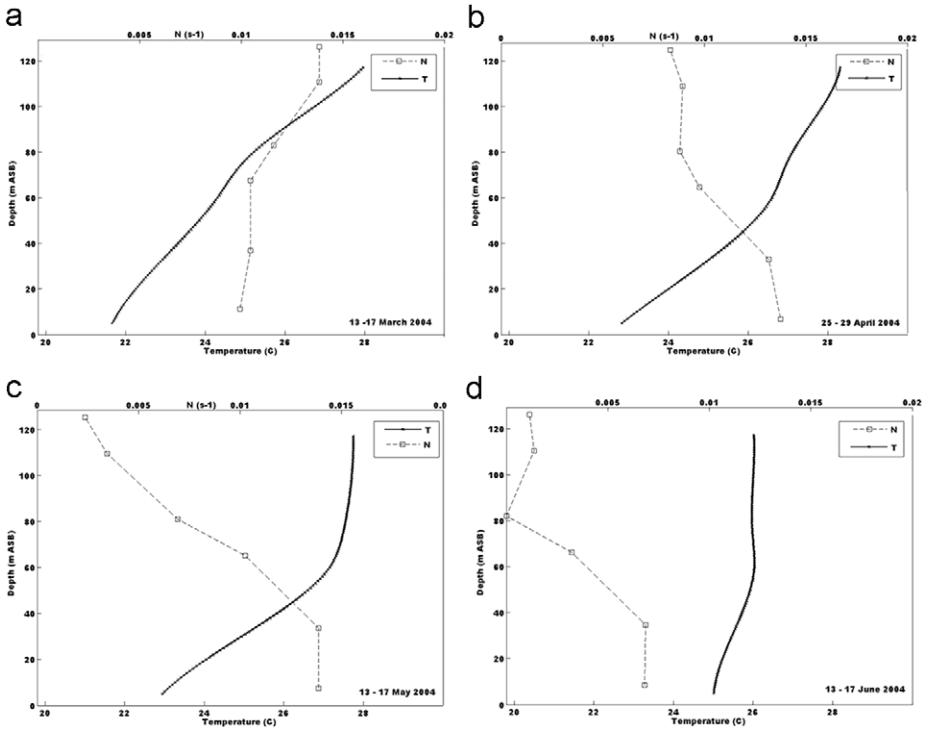

Fig. 4. Background temperature and buoyancy frequency profiles at North Rankin for 5-day averaged time segments in (a) March, (b) April, (c) May and (d) June.

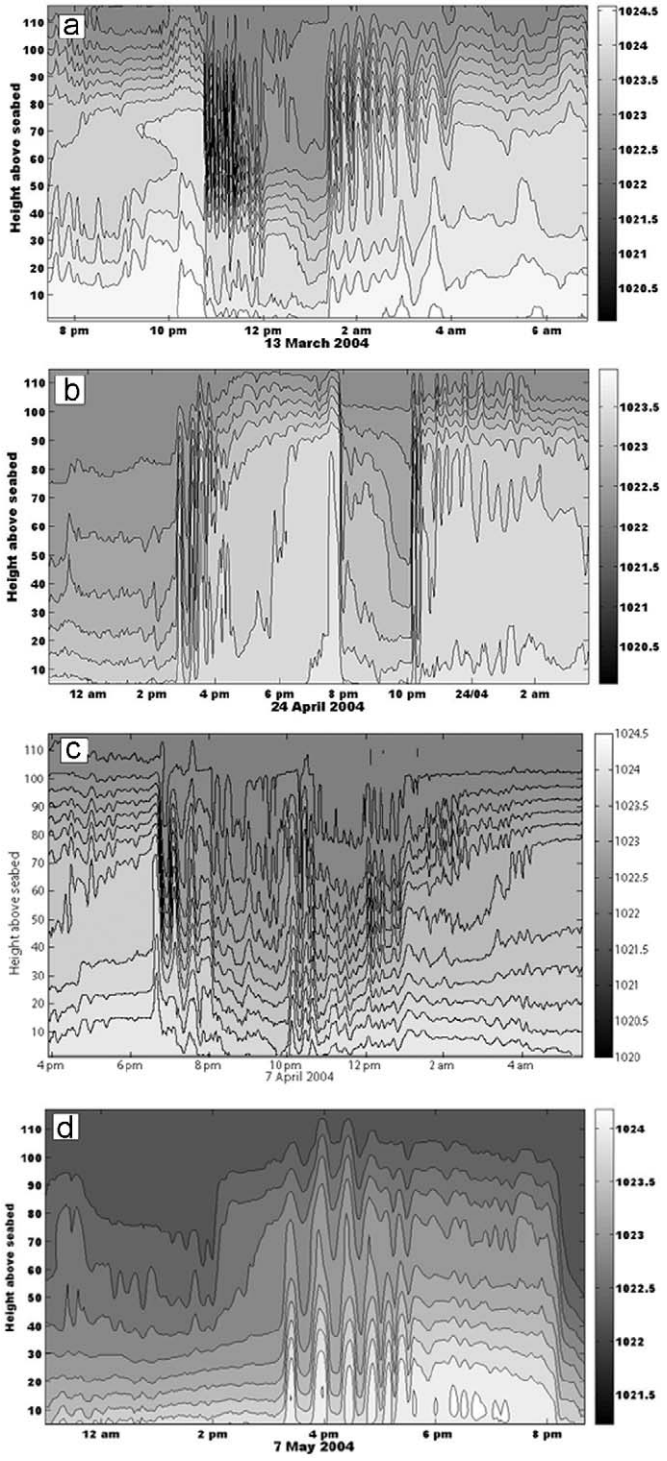

Fig. 5. Contour time series of density profiles of (a) shock waves observed on the 13th of March, (b) 24th of April, (c) triangular-shaped waveform observed on the 7th of April and (d) long-period individual nonlinear internal waves observed on the 7th of May.

To examine the LAIW, we focused on those events which induced current speeds in excess of a threshold defined as 40 cm/s at a depth of 5 m above the sea bottom. This classification resulted in 25 significant events during our deployment period—about 12% of all tidal cycles in the total record. For each event the density profile, linear phase speed, observed phase speed, direction of propagation and the amplitude of the leading wave in a packet were estimated. In order to remove both the low-frequency tidal and circulation signals and the turbulence signal, velocities were band-pass filtered between 10 min and 3 h in order to focus on induced currents associated only with the LAIW packets.

An estimate of the linear phase speed for the first vertical mode was obtained by solving the linear eigenvalue problem given by

$$\frac{d^2\zeta}{dz^2} + \zeta k^2 \left[\frac{N^2(z) - \sigma^2}{\sigma^2 - f^2}\right] = 0 \quad (1)$$

where ζ indicates the vertical displacement, σ is the wave frequency, k is the horizontal wave number, f is the inertial frequency and N is the buoyancy frequency. For a given stratification, water depth, wave and inertial frequency, Eq. (1) can be solved numerically, to give the vertical structure ζ and horizontal wave number k, and hence the linear phase speed of the wave. The buoyancy frequency was calculated from low-pass filtered 24-h averages of the temperatures just before the arrival of a packet. Following Holloway et al. (1997) we assume here negligible dependence on the background shear in this region of the NWS, that the energy is in the first vertical mode, and that bottom slopes are too small to significantly affect the linear phase speed.

The observed phase speed of the packets was calculated by dividing the distance between the moorings on the cross-shore array by the time lag between the arrivals of the leading wave, correcting where necessary when the phase velocity was not aligned directly with the long axis of the array. The phase speeds were finally corrected from advective effects via subtraction the barotropic component of velocity obtained from the flare tower mooring. Using the L-shaped array, the actual direction of propagation of the LAIW packets was analysed carefully for 25 events during the mooring period and the results for phase speed and direction are shown in Fig. 7a and b, respectively. Observed phase speeds were up to twice the linear speed emphasing the strongly nonlinear nature of the LAIWs. During spring tide, the wave packets propagate from a 300° to 335° direction, while during neap tide they propagate from a more northerly direction in the 320–355° range, indicating the waves would not be well described by a simple 2-dimensional (x–z) model.

Finally we took the vertical displacement associated with the leading edge of the wave packet (cf. New and Pingree, 1992; Stanton and Ostrovsky, 1998; Holloway et al., 1999) and calculated the non-dimensional ratio of isotherm displacement of the leading wave to the initial depth, or nonlinearity index as used by Stanton and Ostrovsky (1998). As seen in Fig. 8a, phase speed increases with amplitude of the leading wave and as seen in Fig. 8b the nonlinearity index ranges between 0.6 and 10.4 for our LAIW packets at NRA. The wave of depression observed on 16th March contains the largest vertical displacement observed in this study: a maximum vertical displacement of the isopycnals of 83 m from an initial depth of 8 m, implying an index of value of 10.4 ± 1.5, where the error bounds are our estimate to account for interpolation errors.

Henyey (1999) found that for values of the index less than 0.1, the KdV equation works fairly well, but by the time the parameter reaches 0.2, the KdV equation is unable to describe the dynamics. The extended KdV model accounts for a higher degree of nonlinearity, although formally it also assumes small displacements (Stanton and Ostrovsky, 1998). Grimshaw et al. (2004) used the variable-coefficient extended KdV equation to show that internal solitary wave propagation on the NWS may be well

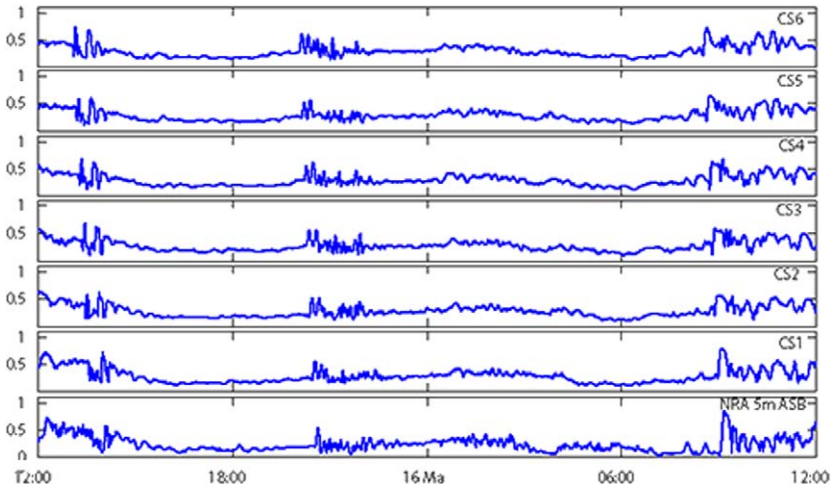

Fig. 6. Typical current signatures as measured during the passage of internal wave packets through the L-shaped array over three tidal cycles on 16th May.

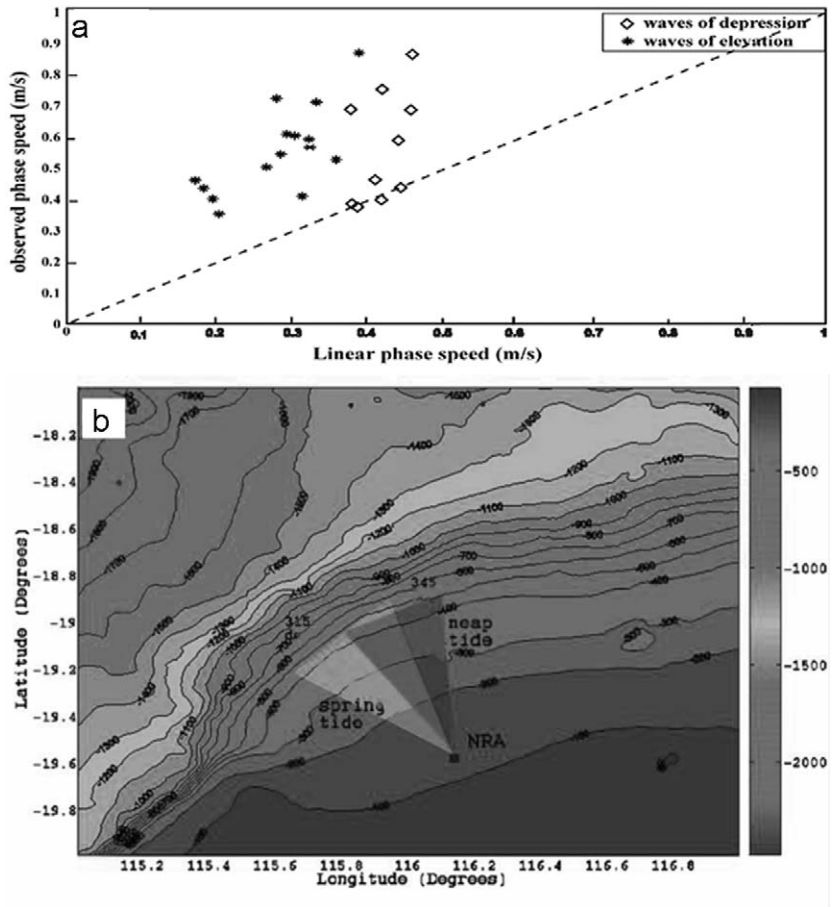

Fig. 7. For 25 events during the mooring period (a) relationship between the linear phase speed and observed phase speed; (b) bathymetric map of the NRA field region showing the range of propagation directions of the LAIW packets associated with spring–neap cycle modulation for the 25 events observed during the mooring period. All events were propagating across a 40° arc bounded by the bearings 315°TN and 355°TN.

described up to a depth of 160 m, but further inshore the applicability of the extended KdV equation becomes questionable due to the large amplitude of the waves. As seen in Fig. 8b for our observation site in 124 m of water, the nonlinearity index lies between 0.6 and 10.4 indicating even the extended KdV is of limited use in describing the observed waves.

3.2. Numerical modeling

We focus in this paper on two issues in regard to the ROMS predictions: first, how does it compare with the observations described above; and second, what can the model tell us about the generation of the internal waves that are observed at the NRA field

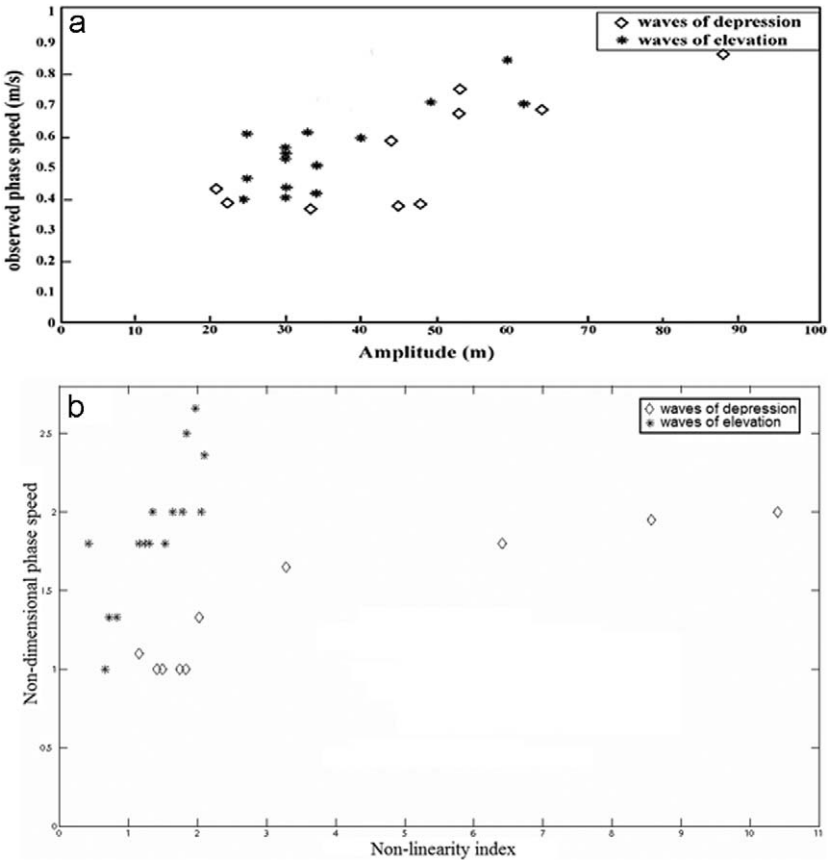

Fig. 8. Relationship between the observed phase speed and the amplitude of the leading wave (a), and the non-dimensional phase speed and the nonlinearity index (b).

site? In particular, our interest is in the model predictions regarding the generation and the evolution dynamics of the internal tide, the influence of the bottom topography and its three-dimensional variability on the internal wave field. The bottom slopes on the continental slope region offshore are a maximum of only 1°, any wave beams generated are thus also of very low slope. It can be shown that the process of generation of the beams is thus hydrostatic to excellent approximation and hence should be well modeled by a hydrostatic model like ROMS. Although the model solution does not have the spatial resolution to resolve the LAIWs seen at NRA and, even more fundamentally, the hydrostatic assumption limits the model's ability in capturing the highly nonlinear behaviour associated with the passage of these waves through NRA (see Fig. 7), the model should resolve linear wave structures associated with the internal tide of wavelengths greater than 20 km. As the shoreward propagating internal tide begins to feel the seabed, nonlinear effects subsequently begin to dominate and the formation, propagation and modification of the IWs can then only be resolved using a non-hydrostatic model. We examine the differences between hydrostatic and a non-hydrostatic solution in Van Gastel et al. (2009).

In Fig. 9A we show a comparison of the predicted and observed sea surface heights at the NRA location over a 30-day period covering two spring–neap cycles. As can be seen, the tidal amplitudes at the site are up to 1.5 m and the modeled response predicts these observed peak amplitudes with an accuracy of ± 0.06 m (one standard deviation). And the correct phasing between model and observation is reproduced. Fig. 9B shows the comparison between the predicted and observed barotropic currents at NRA. To within the 95% confidence intervals shown, the model is in good agreement with the observed currents from low frequencies up to a frequency of approximately $7 \times 10^{-4}\,s^{-1}$, or a period of oscillation of 0.39 h. Finally, Fig. 9C shows the comparison of the percentage exceedance currents between model and data, and shows that the model underestimates the observed magnitude to a maximum of 12% at the peak exceedance level of 95%. Overall, these different comparisons of model and data indicate excellent predictive capability of the barotropic flow at the experimental site.

Fig. 10 shows the spectral comparisons between model and observations at four differing depths for total current, two in the upper water column (Fig. 10A and B) and two near the seabed (Fig. 10C and D). At the 95% confidence interval, for all depths there is good agreement for frequencies up to $3 \times 10^{-4}\,s^{-1}$, or a period of oscillation of ~1 h (~6 times the buoyancy period). Beyond this frequency the model underpredicts the observed currents due to its inability to model the LAIWs that exist in this bandwidth. Finally, in Fig. 11 we show the percent exceedance criteria and note that the model underpredicts the observed total current speed by ~10% over the water column, with the exception of 5 m ASB where the model overpredicts by 5%. We suspect this last effect is due to the model setup underestimating the bottom drag coefficient—note we have used a standard $C_D = 2.5 \times 10^{-3}$ in all simulations. Overall we thus conclude the model is in good agreement with the observations at our experimental site.

Consider now the model predictions regarding internal tide generation offshore of NRA on the continental slope where, although not shown, we know critical points for the M_2 tide do

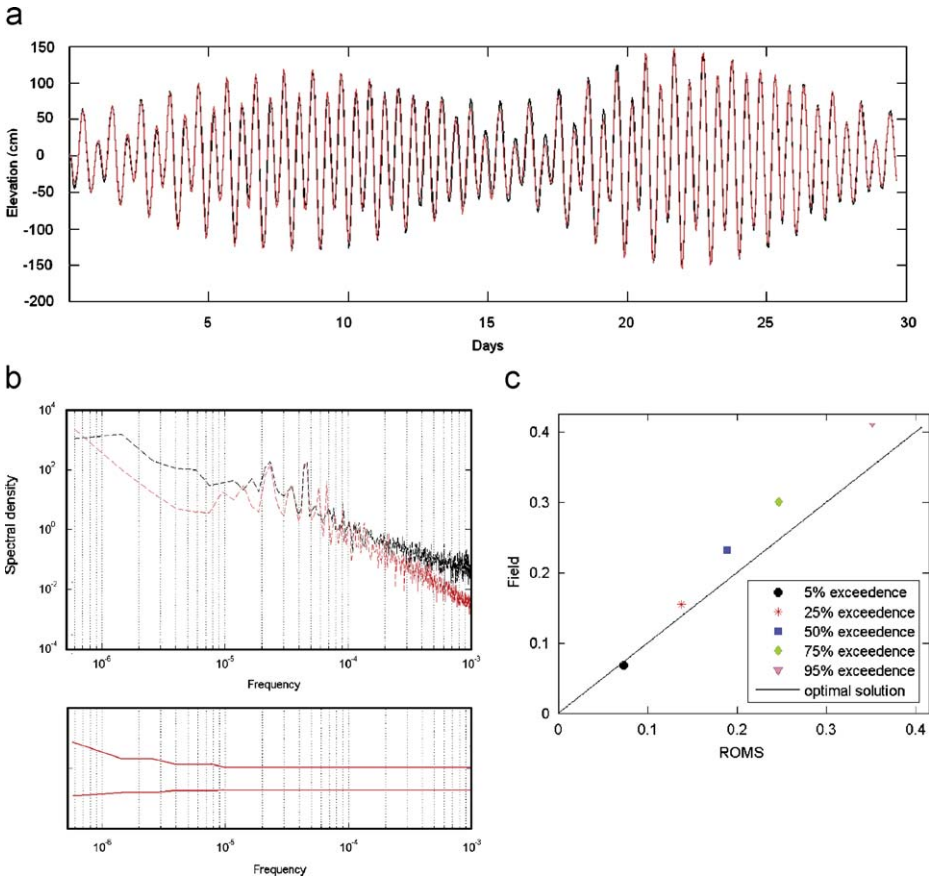

Fig. 9. Model verification: plot A is a time-series comparison of the modeled (dashed red line) and observed (dashed black line) sea surface height (m) variability using converted pressure readings taken adjacent to the NRA platform during January 2000. For comparison purposes only a verification simulation with the same setup as the primary run was performed to coincide with the observation period. Observed pressure data was not available during the period of the primary simulation. Plots B and C refer to verification of the primary simulation. Plot B is the spectral density comparison of the depth averaged total current speed with the 95% confidence interval (solid red line) displayed at the base of the plot, and plot C is the percentage exceedance comparison. The observed depth averaged current speed was determined by averaging the depth integrated current speed recordings at the six current meter locations. (For interpretation of the references to colour in this figure legend, the reader is referred to the web version of this article.)

occur. For clarity, we focus on just a few tidal cycles and show in Fig. 12 the horizontal temperature field extracted from a depth of 60 m every 4 h for a total of 20 h. Each plot clearly shows wave crests (dark to light blue areas) as regions of colder water (23–26 °C) and wave troughs (orange to red area) as regions of warmer water (27.5–29 °C). Consider the region around NRA. The primary internal wave represented by the largest vertical excursion of the isotherms originates from a bearing of 308° (Fig. 12A). A smaller secondary internal wave originates from a bearing of 15° (Fig. 12A) and both waves arrive in phase at NRA. This single wave crest subsequently moves steadily inshore until by Fig. 12D it has propagated all the way to NRA, subsequently moving another 30 km inshore and dissipating in a water depth of about 60 m. A more detailed discussion of the modeling and the dynamics of the internal tide and the effects of topography are given in Van Gastel et al. (2009).

To determine the time of travel from the generation site we extracted a time series of the total velocity along the vertical profile orientated at the same bearing as the primary internal wave. Fig. 13 is a representative vertical profile of the velocity field and shows internal wave generation occurred in depths between 400 and 600 m at 65–75 km from NRA. Internal wave beams originating at the slope forward reflected off both the sea surface and upper the thermocline and showed peak velocities of 0.6 m/s and the beam aspect ratio to be approximately 1:50 (V:H) (Fig. 13).

Model simulations over many tidal cycles show that the internal tide generation appears to occur ~70 km from NRA in an arc ranging from 300° to 15° and extending ~120 km along the (curved) slope and it takes approximately 3.2 tidal cycles for an internal tide to travel from the generation region to NRA. If we take typical *observed* phase speeds of a wave through the L-shaped array as seen in Fig. 7, the inferred travel distance over three tidal cycles yields an estimate of 65 ± 20 km during the spring tide and 75 ± 25 km during a neap tide event. Thus both field data and model are in agreement in predicting that wave generation occurs in water depth of 400–600 m. Fig. 12 clearly shows not only the spatial extent over which internal tide generation occurs but, due to the curved nature of the bathymetry, a focusing of the baroclinic energy towards NRA. This form of topographical steering thus plays an important role in the observed tidal dynamics at NRA and highlights the importance of 3D numerical models in determining the propagation characteristics of the wave paths.

4. Conclusions

The data from this study at the NRA gas production platform in 124 m of water shows an internal wave field characterized by very energetic LAIWs over the entire 3.5-month period from summer to winter conditions. Waves are strongest and are

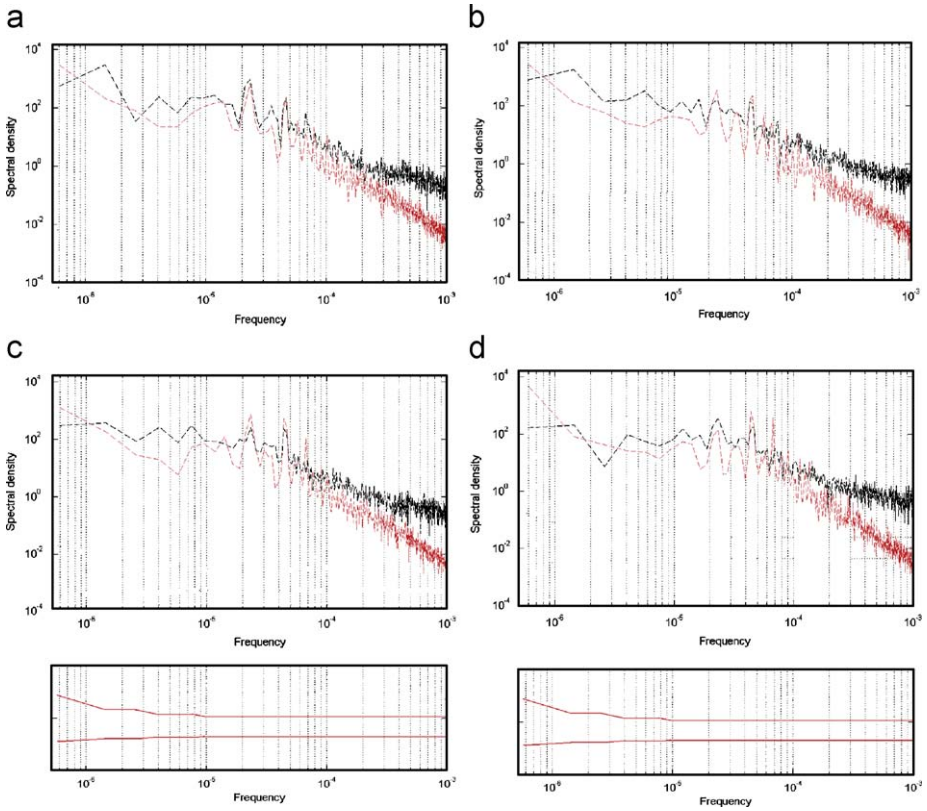

Fig. 10. Spectral density comparison of the modeled (dashed red line) and observed (dashed black line) total current speed (m/s). Plot A at 117 m ASB, plot B at 75 m ASB, plot C at 30 m ASB and plot D at 5 m ASB. At the base of each column is the correctly scaled 95% confidence interval (solid red line) applicable to each of the spectral plots. (For interpretation of the references to colour in this figure legend, the reader is referred to the web version of this article.)

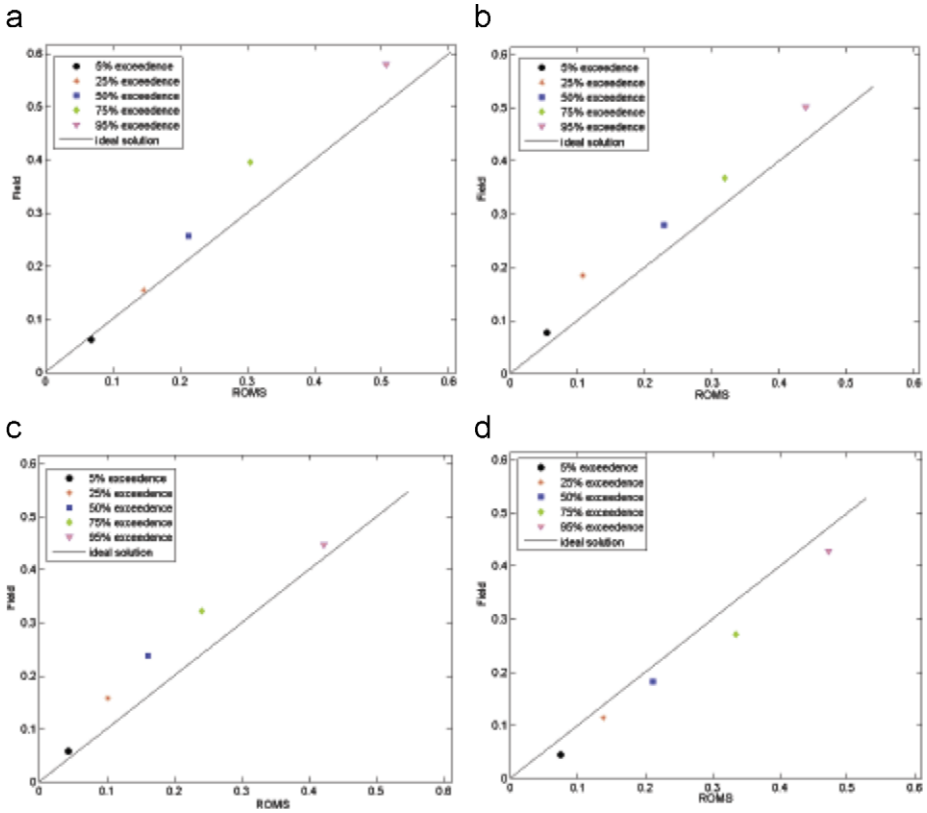

Fig. 11. Percentage exceedance at 5%, 25%, 50%, 75% and 95% of the modeled (ROMS) vs. observed (Field) total current speed (m/s). Plot A at 117 m ASB, plot B at 75 m ASB, plot C at 30 m ASB and plot D at 5 m ASB.

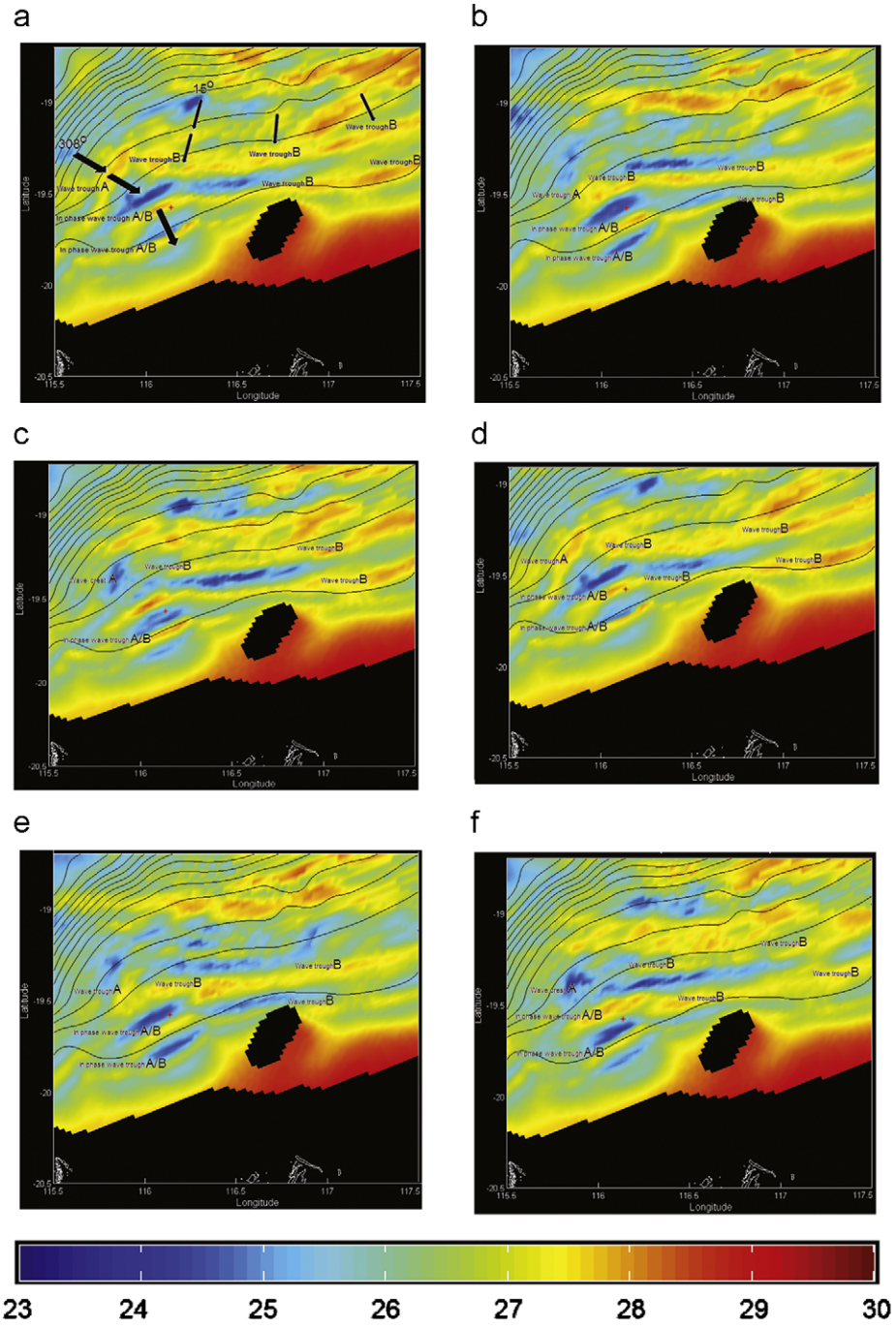

Fig. 12. Time series of the horizontal temperature slice at a depth of 60 m. The time interval between each snapshot is 4 h commencing on the 24th of March, 2004. Plot A at 12 a.m. the 24th of March, 2004, plot B 4 a.m. the 24th of March, 2004, plot C 8 a.m. the 24th of March, 2004, plot D 12 p.m. the 24th of March, 2004, plot E 4 p.m. the 24th of March, 2004 and plot F 8 p.m. the 24th of March, 2004. The location of NRA is given by the red asterisk. The black areas represent land. (For interpretation of the references to colour in this figure legend, the reader is referred to the web version of this article.)

predominantly waves of depression during the summer, while in winter they are weaker and are predominantly waves of elevation. The application of the nonlinearity index over the study period reveals an internal wave field characterized by strong nonlinearity, suggesting that even the less energetic waves are unlikely candidates for a description based on weakly nonlinear theory. For the first time, we were able to accurately measure the phase speed and direction of propagation of the wave packets without ambiguity. The phase speed of the NIW packets depends on the seasonal variability in stratification at the shelf break, but also is sensitive to any large scale flow variability. The variation from spring to neap tide affects the observed direction of propagation of the wave packets. The generation site for the waves has been estimated in a water depth of some 400–600 m.

The numerical simulations predicted tidal beams emanating from critical topography on the slope and showed the focusing of internal tidal energy towards the NRA site.

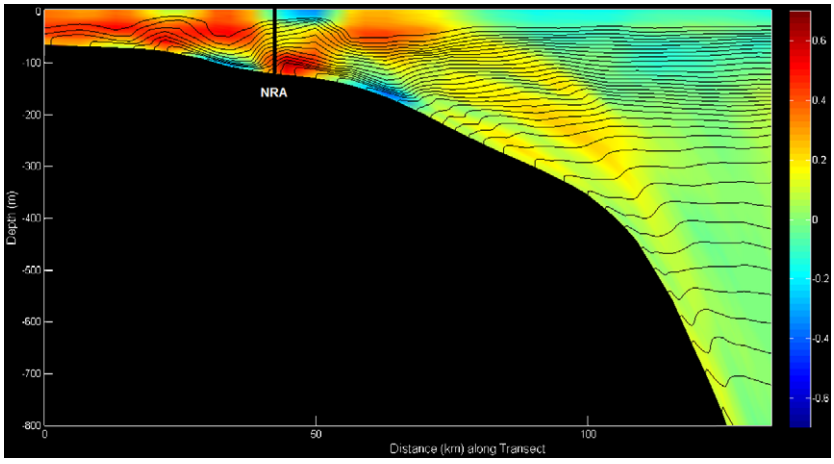

Fig. 13. Snapshot of the vertical profile of the total current speed (colour) overlaid with isotherms (thin black lines) at a bearing 315° or along the same bearing as the primary internal wave illustrated in Fig. 12. The time of the snapshot is 12 a.m. the 24th of March, 2004. Clearly evident are the internal wave beams and their forward reflection off both the sea surface and upper thermocline. (For interpretation of the references to colour in this figure legend, the reader is referred to the web version of this article.)

Acknowledgements

The measurement data and the analysis work in this paper are part of ongoing Woodside Energy Ltd. funded research into internal waves off North West Australia. The authors wish to thank Stan Stroud of Woodside Energy Ltd. for funding this program and for permission to use these data. The data were collected by Metocean Engineers Pty Ltd., under the direction of Steve Buchan, under contract to Woodside. We also wish to thank the Western Australian Interactive Virtual Environments Centre (IVEC) for access to the SGI high-performance computer (COGNAC). Additional funding was supplied by the West Australian Marine Science Institute (WAMSI). PVG acknowledges the support provided by International Postgraduate Research Scholarship (IPRS). Kraig Winters, Marco Ghisalberti and Geoff Wake offered helpful comments on earlier drafts and Lorraine Dorn helped in generating the figures.

References

Baines, P.G., 1981. Satellite observations of internal waves on the Australian North West Shelf. J. Mar. Freshwater Res. 32, 457–463.
Craig, P.D., 1988. A numerical model study of internal tides on the Australian North West Shelf. J. Mar. Res. 46, 59–76.
Egbert, G.D., Ray, R.D., 2000. Significant dissipation of tidal energy in the deep ocean inferred from satellite altimeter data. Nature 405, 775–778.
Grimshaw, R., Pelinovsky, E., Kurkin, A., Talipova, T., 2004. Simulation of the transformation of internal solitary waves on oceanic shelves. J. Phys. Oceanogr. 34, 2774–2791.
Haidvogel, D.B., Arango, H.G., Hedstrom, K., Beckmann, A., Malanotte-Rizzoli, P., Shchepetkin, A.F., 2000. Model evaluation experiments in the North Atlantic Basin: simulations in nonlinear terrain-following coordinates. Dyn. Atmos. Oceans 32, 239–281.
Henyey, F.S., 1999. Exact Solitary Wave Solutions in Shallow Water. Aha Huliko'a Hawaiian Winter Workshop 1999, pp. 89–93.
Holloway, P.E., 1983. Internal tides on the Australian North-West Shelf: a preliminary investigation. J. Phys. Oceanogr. 13, 1357–1370.
Holloway, P.E., 1984. On the semidiurnal internal tide at a shelf-break region on the Australian North West Shelf. J. Phys. Oceanogr. 14, 1787–1799.
Holloway, P.E., 1987. Internal hydraulic jumps and solitons at a shelf break region on the Australian North West Shelf. J. Geophys. Res. 92 (C5), 5405–5416.
Holloway, P.E., 1996. A numerical model of internal tides with application to the Australian North West Shelf. J. Phys. Oceanogr. 26, 21–37.
Holloway, P.E., Pelinovsky, E., Talipova, T., Barnes, B., 1997. A nonlinear model of internal tide transformation on the Australian North West Shelf. J. Phys. Oceanogr. 27, 871–896.
Holloway, P.E., Pelinovsky, E., Talipova, T., 1999. A Generalized Korteweg–de Vries model of internal tide transformation in the coastal zone. J. Geophys. Res. 104, 18333–18350.
Holloway, P.E., Chatwin, P.G., Craig, P.D., 2001. Internal tide observations from the Australian North West Shelf in summer 1995. J. Phys. Oceanogr. 31, 1182–1199.
Huthnance, J.M., 1989. Internal tides and waves near the continental shelf edge. Geophys. Astrophys. Fluid Dyn. 48, 81–106.
Mellor, G.L., Yamada, T., 1982. Development of a turbulence closure model for geophysical fluid problems. Rev. Geophys. 20, 851–875.
New, A.L., Pingree, R.D., 1990. Large-amplitude internal soliton packets in the central Bay of Biscay. Deep-Sea Res 37, 513–524.
New, A.L., Pingree, R.D., 1992. Local generation of internal soliton packets in the central Bay of Biscay. Deep-Sea Res. 39, 1521–1534.
Oke, P.R., Brassington, G., Griffin, D.A., Schiller, A., 2008. The Bluelink ocean data assimilation system. Ocean Modelling 21, 46–70.
Shchepetkin, A.F., McWilliams, J.C., 2005. The Regional Ocean Modeling System: a split-explicit, free-surface, topography-following coordinates ocean model. Ocean Modelling 9, 347–404.
Smyth, N.F., Holloway, P.E., 1988. Hydraulic jump and undular bore formation on a shelf break. J. Phys. Oceanogr. 18, 947–962.
Stanton, T.P., Ostrovsky, L.A., 1998. Observations of highly nonlinear internal solitons over the continental shelf. Geophys. Res. Lett. 25, 2695–2698.
Van Gastel, P., Meuleners, M., Ivey, N., Fringer, O., 2009. Energetics of internal waves on the Australian North West Shelf. Cont. Shelf Res., in preparation.
Vlasenko, V., Stashchuk, N., Hutter, K., 2005. Baroclinic Tides: Theoretical Modeling and Observational Evidence. Cambridge University Press.
Vlasenko, V., Stashchuk, N., 2007. Three-dimensional shoaling of large amplitude internal waves. J. Geophys. Res. 112 (C1108), 1–15.